Closed-Loop Fidelity Assessment of Linear Time-Invariant Helicopter Models for Rotor and Flight Control Interaction Studies

Ashwani K. Padthe
Postdoctoral Researcher
akpadthe@umich.edu

Peretz P. Friedmann
François-Xavier Bagnoud Professor
peretzf@umich.edu

Department of Aerospace Engineering
University of Michigan
Ann Arbor, MI 48109
Ph : (734) 763-2354

Abstract

Linearized time-periodic models are extracted from a high fidelity comprehensive nonlinear helicopter model at a low-speed descending flight condition and a cruise flight condition. A Fourier expansion based model reduction method is used to obtain linearized time-invariant models from the time-periodic models. These linearized models are intended for studies examining the interaction between on-blade control and the primary flight control system. On-blade control is usually implemented in closed-loop mode, therefore, the LTI models are verified for closed-loop performance fidelity. The higher harmonic controller is used with the 2/rev-5/rev harmonic components of the flap deflection as the control input and vibratory hub loads as the output. Closed-loop performance of the LTI model is compared to that of the nonlinear model at both low-speed descending flight and cruise flight conditions. The flap deflection histories and the vibratory loads predicted using the LTI model and nonlinear model agree very well at both the flight conditions when the flap deflection is limited to be less than 2°. The errors between the two models increase with an increase in the flap deflection amplitude. Overall, the results show that the linearized time-invariant models are suitable for studying closed-loop on-blade vibration control and the interactions with the primary flight control system.

Nomenclature

$\mathbf{A}(\psi), \mathbf{B}(\psi),$ $\mathbf{C}(\psi), \mathbf{E}(\psi)$	Matrices in the linear time-periodic model
$\mathbf{A}_{21}, \mathbf{A}_{22},$ $\mathbf{A}_{23}, \mathbf{A}_{31},$ $\mathbf{A}_{32}, \mathbf{A}_{33},$ $\mathbf{B}_2, \mathbf{B}_3, \mathbf{C}_2,$ $\mathbf{C}_3, \mathbf{E}_1$	Matrices in the linear time-invariant model
C_W	Helicopter weight coefficient
$\mathbf{D}_a$	$= -\frac{\partial \mathbf{h}_a}{\partial \dot{\mathbf{x}}_s}$
$\mathbf{D}_s$	$= -\frac{\partial \mathbf{h}}{\partial \dot{\mathbf{x}}_a}$
$\mathbf{f}$	Output function relating the hub loads to the blade structural and aerodynamic degrees of freedom
f	Equivalent flat plate area of the fuselage
$\mathbf{h}$	Function representing blade structural equations of motion in terms of rotating coordinates
$\mathbf{h}_a$	Function representing blade aerodynamic equations of motion in terms of rotating coordinates
$\mathbf{G}_a$	$= \frac{\partial \mathbf{h}_a}{\partial \mathbf{u}}$
$\mathbf{G}_s$	$= \frac{\partial \mathbf{h}}{\partial \mathbf{u}}$
$\mathbf{g}$	Function representing blade structural equations of motion in terms of multi-blade coordinates
$\mathbf{g}_a$	Function representing blade aerodynamic equations of motion in terms of multi-blade coordinates
$\mathbf{K}_{aa}$	$= -\frac{\partial \mathbf{h}_a}{\partial \mathbf{x}_a}$
$\mathbf{K}_{as}$	$= -\frac{\partial \mathbf{h}_a}{\partial \mathbf{x}_s}$

$\mathbf{K}_{sa}$	$= -\frac{\partial \mathbf{h}}{\partial \mathbf{x}_a}$
$\mathbf{K}_{ss}$	$= -\frac{\partial \mathbf{h}}{\partial \mathbf{x}_s}$
M_b	Blade mass
N_b	Number of rotor blades
$\mathbf{P}_a$	$= \frac{\partial \mathbf{f}}{\partial \mathbf{x}_a}$
$\mathbf{P}_s$	$= \frac{\partial \mathbf{f}}{\partial \mathbf{x}_s}$
$\mathbf{Q}$	$= \frac{\partial \mathbf{f}}{\partial \dot{\mathbf{x}}_s}$
$\mathbf{R}$	$= \frac{\partial \mathbf{f}}{\partial \mathbf{u}}$
R	Rotor blade radius
$\mathbf{u} = \{\mathbf{u}_1, \mathbf{u}_2, \mathbf{u}_3, \mathbf{u}_4\}'$	Individual blade coordinates representing flap deflection/control inputs
$\mathbf{u}_{\text{aug}}$	Augmented input vector used in the LTI model
$\mathbf{x}_{\text{aug}}$	Augmented state vector used in the LTI model
$\mathbf{u}_m = \{\mathbf{u}_{m0}, \mathbf{u}_{m1c}, \mathbf{u}_{m1s}, \mathbf{u}_{m2}\}'$	Multi-blade coordinates representing flap deflection/control inputs
X_{FA}, Z_{FA}	Longitudinal and vertical offsets between rotor hub and helicopter aerodynamic center
X_{FC}, Z_{FC}	Longitudinal and vertical offsets between rotor hub and helicopter center of gravity
$\mathbf{x}_s = \{\mathbf{x}_1, \mathbf{x}_2, \mathbf{x}_3, \mathbf{x}_4\}'$	Rotating blade coordinates representing blade deflections in the rotating coordinate system
$\mathbf{x}_a = \{\mathbf{x}_{a1}, \mathbf{x}_{a2}, \mathbf{x}_{a3}, \mathbf{x}_{a4}\}'$	Rotating blade coordinates representing the aerodynamic states in the rotating coordinate system
$\mathbf{x}_{ms} = \{\mathbf{x}_{m0}, \mathbf{x}_{m1c}, \mathbf{x}_{m1s}, \mathbf{x}_{m2}\}'$	Multi-blade coordinates representing blade deflections in the non-rotating coordinate system
$\mathbf{x}_{ma} = \{\mathbf{x}^a_{m0}, \mathbf{x}^a_{m1c}, \mathbf{x}^a_{m1s}, \mathbf{x}^a_{m2}\}'$	Multi-blade coordinates representing aerodynamic states in the non-rotating coordinate system
$\mathbf{x}^0_{m0}, \mathbf{x}^0_{m1c}, \mathbf{x}^0_{m1s}, \mathbf{x}^0_{m2}$	Multi-blade coordinates corresponding to the periodic equilibrium
$\mathbf{y}$	Output vector
$\mathbf{y}_{\text{aug}}$	Augmented output vector used in the LTI model
α_{D}	Descent angle
α_{R}	Rotor shaft angle
β_p	Blade precone angle
γ	Lock number
δ	Flap or microflap deflection
Δ	Symbol indicating a perturbation
ϕ_{R}	Lateral roll angle
μ	Advance ratio
θ_0	Collective pitch
θ_{0t}	Tail rotor pitch angle
θ_{1c}, θ_{1s}	cyclic pitch components
θ_{tw}	Blade pretwist distribution
σ	Rotor solidity
$\omega_F, \omega_L, \omega_T$	Blade flap, lag and torsional natural frequencies
Ω	Rotor angular speed
ψ	Azimuth angle
ζ	Output vector in the LTP model
ξ	State variable vector in the LTP model
υ	Input vector in the LTP model
$()^0$	Superscript indicating the average Fourier coefficient
$()^{ic}$	Superscript indicating the i^{th} cosine Fourier coefficient
$()^{is}$	Superscript indicating the i^{th} sine Fourier coefficient
ACF	Actively-Controlled Flaps
AVINOR	Active Vibration and Noise Reduction
FEMR	Fourier-Expansion based Model Reduction
HFC	Helicopter Flight Control
HHC	Higher Harmonic Control
LTI	Linear Time-Invariant
LTP	Linear Time-Periodic
OBC	On-Blade Control
RFA	Rational Function Approximation
RMS	Root Mean Square

1 Introduction

Vibration and noise reduction in rotorcraft using active control has been a major area of research during the last three decades. In addition to causing crew and passenger discomfort, vibrations reduce the airframe and component fatigue life and limit rotorcraft performance resulting in high maintenance costs. High noise levels limit community acceptance of rotorcraft for civilian applications and

also affect military helicopter detection. On-blade active control (OBC) approaches, such as the actively controlled plain trailing-edge flaps (ACF) [1–3] and the microflaps [4] have been explored for rotorcraft vibration and noise reduction as well as performance enhancement. However, the influence of these OBC systems on the helicopter flight control systems (HFC) and its handling qualities has received attention only recently [5]. Understanding the interaction between high-bandwidth control using OBC systems and the closed-loop flight control systems is an essential pre-requisite to OBC implementation on a production helicopter.

The handling qualities specifications for small amplitude maneuvers prescribed in Aeronautical Design Standard (ADS-33, [6]) are based on linear time-invariant (LTI) model specifications. Furthermore, LTI models provide a convenient framework for control system design. Thus, extraction of a LTI approximation of the helicopter dynamics is an essential step towards carrying out an OBC and HFC interaction study. The first step in extraction of LTI models is to obtain a linearized time-periodic (LTP) model by linearizing the nonlinear model about a periodic equilibrium. Subsequently, LTI models are extracted from the LTP model. Various methods, such as the Lyapunov-Floquet transformation method, Hill's method, time-lifting and frequency-lifting methods [7] have been explored in the literature for reformulation of LTP models into LTI form. The Hill's method in which the LTI models are extracted using a Fourier expansion of the LTP model matrices has been found to provide a convenient framework for higher-harmonic control and flight control interaction studies in helicopters [5,8,9]. In Ref. 8, Hill's method was used to extract LTI helicopter model approximations that can capture the N/rev vibratory hub load dynamics, where N is the number of rotor blades. The LTI models can only predict the perturbations in vibratory loads about a periodic equilibrium. Interactions between a conventional higher harmonic control (HHC) system and the HFC system were studied using the LTI helicopter models. The LTI models were extracted from an existing coupled nonlinear rotor-fuselage model of the Sikorsky UH-60 Black Hawk helicopter based on rigid flap-lag and first torsional degrees of freedom. Quasi-steady compressible aerodynamics and a three-state dynamic inflow model, which yields a linear inflow distribution over the rotor-disk were used in the nonlinear model. The conventional HHC controller was used to minimize the N/rev vibratory hub loads. Implementing the HHC controller in closed-loop had a negligible effect on the AFCS performance and overall handling qualities, indicating the lack of dynamic coupling of HHC into flight control. However, a significant vibration response to pilot inputs was noticed. The open-loop vibratory shears were increased by more than 100% during a rolling maneuver. Performance of the HHC system in suppressing transient vibration response during the rolling maneuver was examined. The root-mean-square vibration shears were reduced by 30% using an enhanced HHC system. It should be noted that this study only provides a framework for estimating mutual interactions between the vibratory hub loads and the flight mechanics. However, due to the primitive nature of the rotor structural and aerodynamic models used, only qualitative conclusions can be drawn.

Another method for the extraction of LTI helicopter models from a nonlinear model was developed in Ref. 9. The method involves a two-step approach where a LTP model is extracted from a nonlinear model using a numerical perturbation scheme. Subsequently, a Fourier expansion based harmonic decomposition of the LTP model matrices is used to arrive at a LTI model of selected order. This method is refered to as the Fourier expansion based model reduction (FEMR) approach in this paper. Fidelity of the LTI models to the LTP models was assessed in Ref. 9. Methodologies to reduce the LTI model order while retaining the fidelity of the full-order LTI model were developed in Ref. 10. The nonlinear helicopter model used in these studies was the generic helicopter model embedded in FLIGHTLAB and includes one rigid plus one elastic mode for flap as well as lead-lag motions of each blade and a 15-state dynamic inflow model. The blade feathering is assumed to be rigid. These LTI models were used in Ref. 11 to develop an advanced control system based on dynamic crossfeeds that can mitigate the vibration response during a maneuvering flight. The classical higher harmonic controller was used in this study. The nonlinear helicopter simulation models used in the studies mentioned earlier are adequate for capturing only the 1^{st} order dynamic effects. However, these are not sufficient for accurate predictions of vibratory hub loads. Furthermore, the codes used did not account for the presence of on-blade control systems. Recently, in Ref. [5], the FEMR approach was used to extract LTP and LTI models from a high fidelity nonlinear helicopter model embedded in the AVINOR (Active Vibration and Noise Reduction) code [12]. The nonlinear model accounts for higher-order structural

dynamic effects, dynamic stall effects, non-uniform inflow and unsteady aerodynamic effects due to on-blade control surfaces, providing an accurate prediction of the vibratory hub loads and the effects of on-blade control devices. The LTP and LTI model hub load responses were validated against the nonlinear model response. Very good agreements were observed with the inclusion of the aerodynamic model states in the linearized models for prescribed open-loop flap inputs. However, on-blade control devices are expected to be implemented in the closed-loop mode. Therefore, to study on-blade control and flight control interactions, it is imperative to develop LTI models that retain the closed-loop characteristics of the nonlinear model. Thus, primary goal of this study is to construct high-fidelity LTP and LTI models that can accurately capture the closed-loop on-blade vibration control characteristics of the nonlinear model. The specific goals of this paper are:

1. Construct high-fidelity LTP and LTI models that can accurately capture the *closed-loop* on-blade control characteristics of a nonlinear helicopter model.
2. Evaluate the LTI model by comparing its *closed-loop* vibration reduction performance and the optimal flap deflection prediction against the nonlinear model when using a plain trailing-edge flap.
3. Construct and evaluate the LTI models at both a low-speed descending flight and a cruise flight condition.

2 Rotorcraft Aeroelastic Analysis Code

The AVINOR comprehensive rotorcraft aeroelastic response code, which has been extensively used to study vibration and noise reduction using flaps and microflaps [1, 4, 12], is employed in this study to extract linearized models. The principal ingredients of the AVINOR code are concisely summarized next.

2.1 Structural dynamic model

The geometrically nonlinear structural dynamic model in AVINOR accounts for moderate blade deflections and fully coupled flap-lag-torsional dynamics for each blade. The structural equations of motion are discretized using the global Galerkin method, based upon the free vibration modes of the rotating blade. The dynamics of the blade are represented by three flap, two lead-lag, and two torsional modes. The code also has the option of modeling the blades using a finite-element method. The effects of control surfaces such as the trailing-edge plain flaps on the structural properties of the blade are neglected. Thus, the control surfaces only influence the blade behavior through their effect on the aerodynamic and inertial loads.

2.2 Aerodynamic model

The blade/flap sectional time-domain aerodynamic loads for attached flow are calculated using a rational function approximation (RFA) based reduced order model constructed from frequency-domain doublet-lattice based aerodynamic data [13]. This model provides unsteady lift, moment, and hinge moment for the plain flap configurations. A more sophisticated CFD based RFA model that can predict drag in addition to lift, moment, and hinge moment due to flaps and microflaps is also available in the code. However, it is not used in this study because it is computationally more expensive. The RFA model is linked to a free wake model [1], which produces a spanwise and azimuthally varying inflow distribution. In the separated flow regime aerodynamic loads are calculated using the ONERA dynamic stall model [12].

2.3 Coupled aeroelastic response/trim solution

The combined structural and aerodynamic equations are represented by a system of coupled ordinary differential equations with periodic coefficients in state-variable form. Propulsive trim, where three force equations (longitudinal, lateral, and vertical) and three moment equations (roll, pitch, and yaw) corresponding to a helicopter in free flight are enforced, is implemented. A simplified tail rotor model, based on uniform inflow and blade element theory, is used. The six trim variables are the rotor shaft angle α_R, the collective pitch θ_0, the cyclic pitch θ_{1s} and θ_{1c}, the tail rotor constant pitch θ_{0t}, and lateral roll angle ϕ_R. The coupled trim/aeroelastic equations are solved in time using a predictor-corrector ODE solver DDEABM, based on the Adams-Bashforth direct numerical integration procedure.

2.4 The Higher Harmonic Control Algorithm

Active control of vibration and noise is implemented using the HHC algorithm, which has been used extensively in rotorcraft applications [1, 14]. The algorithm is based on the assumption that the helicopter can be represented by a linear model relating the output of interest $\mathbf{z}$ to the control input $\mathbf{u}$. The measurement of the plant output and update of the control input are performed at specific times $t_k = k\tau$, where τ is the time interval between updates during which the plant output reaches a steady state. In actual implementation of the algorithm, this time interval may be one or more revolutions. A schematic of the HHC architecture implemented on a helicopter is shown in Fig. 1. The

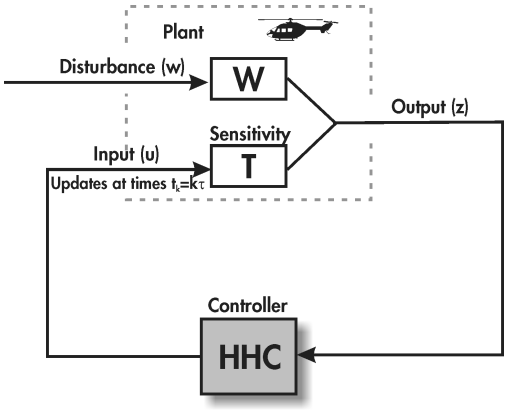

Figure 1: Higher harmonic control architecture

disturbance $\mathbf{w}$ represents the helicopter operating condition. The output vector at the k^{th} time step is given by

$$\mathbf{z}_k = \mathbf{T}\mathbf{u}_k + \mathbf{W}\mathbf{w} \tag{1}$$

where the sensitivity matrix $\mathbf{T}$ represents a linear approximation of the helicopter response to the control and is given by

$$\mathbf{T} = \frac{\partial \mathbf{z}}{\partial \mathbf{u}}. \tag{2}$$

At the initial condition, $k = 0$,

$$\mathbf{z}_0 = \mathbf{T}\mathbf{u}_0 + \mathbf{W}\mathbf{w}. \tag{3}$$

Subtracting Eq. (3) from Eq. (1) to eliminate the unknown $\mathbf{w}$ yields

$$\mathbf{z}_k = \mathbf{z}_0 + \mathbf{T}(\mathbf{u}_k - \mathbf{u}_0). \tag{4}$$

The controller is based on the minimization of a quadratic cost function

$$J(\mathbf{z}_k, \mathbf{u}_k) = \mathbf{z}_k^{\mathrm{T}}\mathbf{Q}\mathbf{z}_k + \mathbf{u}_k^{\mathrm{T}}\mathbf{R}\mathbf{u}_k. \tag{5}$$

The optimal control input is determined from the requirement

$$\frac{\partial J(\mathbf{z}_k, \mathbf{u}_k)}{\partial \mathbf{u}_k} = 0, \tag{6}$$

which yields the optimal control law $\mathbf{u}_{k,\mathrm{opt}}$, given by

$$\mathbf{u}_{k,\mathrm{opt}} = -(\mathbf{T}^{\mathrm{T}}\mathbf{Q}\mathbf{T} + \mathbf{R})^{-1}(\mathbf{T}^{\mathrm{T}}\mathbf{Q})(\mathbf{z}_0 - \mathbf{T}\mathbf{u}_0). \tag{7}$$

This is a classical version of the HHC algorithm that yields an explicit relation for the optimal control input. Another version of the HHC algorithm where the sensitivity matrix $\mathbf{T}$ is updated using least-squares methods after every control update is known as the adaptive or recursive HHC and is discussed in Ref. 14.

In a 4-bladed rotor, the control input $\mathbf{u}_k$ is a combination of 2/rev, 3/rev, 4/rev, and 5/rev harmonic amplitudes of the control surface deflection:

$$\mathbf{u}_k = [\delta_{2c}, \delta_{2s}, ..., \delta_{5c}, \delta_{5s}]^T. \tag{8}$$

The total control surface deflection is given by

$$\delta(\psi, \mathbf{u}_k) = \sum_{N=2}^{5} \left[\delta_{Nc}\cos(N\psi) + \delta_{Ns}\sin(N\psi)\right]. \tag{9}$$

where the quantities δ_{Nc} and δ_{Ns} correspond to the cosine and sine components of the N/rev control input harmonic. For vibration reduction (VR) studies, the output vector $\mathbf{z}_k$ consists of 4/rev vibratory hub shears and moments:

$$\mathbf{z}_{\mathrm{VR}} = \begin{bmatrix} F_{HX4} \\ F_{HY4} \\ F_{HZ4} \\ M_{HX4} \\ M_{HY4} \\ M_{HZ4} \end{bmatrix}. \tag{10}$$

The weighting matrix $\mathbf{Q}$ in the cost function in Eq. 5 is a diagonal matrix. For vibration control, it is described by six weights corresponding to the three vibratory hub shears and the three vibratory hub moments.

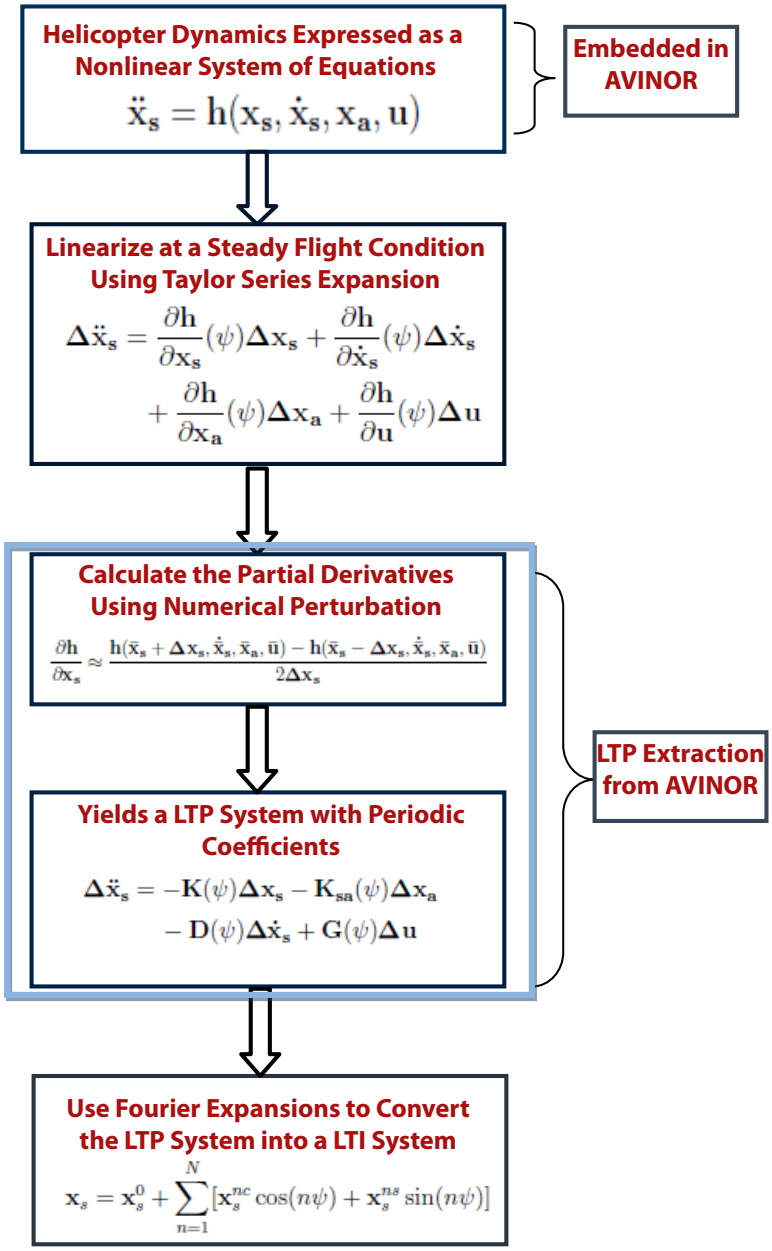

Figure 2: A schematic of the steps involved in extracting linearized models from AVINOR.

3 LTP and LTI model extraction from AVINOR

The procedure for extracting linearized time-periodic and time-invariant models from the nonlinear AVINOR code is briefly described in this section. Details of the extraction procedure can be found in Ref. 5. First, a LTP model is extracted by linearizing the nonlinear model about a trim state. Steps involved are outlined in Fig. 2. The structural equations of motion in the AVINOR code are formulated as

$$\ddot{\mathbf{x}}_s = \mathbf{h}(\mathbf{x}_s, \dot{\mathbf{x}}_s, \mathbf{x}_a, \mathbf{u}) \tag{11}$$

where $\mathbf{x}_s$ is the state variable vector containing the structural degrees of freedom, $\mathbf{x}_a$ is the state variable vector containing the augmented aerodynamic states associated with the RFA aerodynamic model [13], $\mathbf{u}$ is the control input vector, and $\mathbf{h}$ is a general nonlinear function. Linearizing Equation 11 about a periodic equilibrium yields a linear time-periodic system given by

$$\begin{aligned}\Delta\ddot{\mathbf{x}}_s =& \frac{\partial \mathbf{h}}{\partial \mathbf{x}_s}(\psi)\Delta\mathbf{x}_s + \frac{\partial \mathbf{h}}{\partial \dot{\mathbf{x}}_s}(\psi)\Delta\dot{\mathbf{x}}_s + \frac{\partial \mathbf{h}}{\partial \mathbf{x}_a}(\psi)\Delta\mathbf{x}_a \\ &+ \frac{\partial \mathbf{h}}{\partial \mathbf{u}}(\psi)\Delta\mathbf{u}\end{aligned} \tag{12}$$

or

$$\begin{aligned}\Delta\ddot{\mathbf{x}}_s = &-\mathbf{K}_{ss}(\psi)\Delta\mathbf{x}_s - \mathbf{K}_{sa}(\psi)\Delta\mathbf{x}_a - \mathbf{D}_s(\psi)\Delta\dot{\mathbf{x}}_s \\ &+ \mathbf{G}_s(\psi)\Delta\mathbf{u}\end{aligned} \tag{13}$$

where $\Delta\mathbf{x}_s, \Delta\dot{\mathbf{x}}_s, \Delta\mathbf{x}_a, \Delta\mathbf{u}$ represent perturbations in $\mathbf{x}_s, \dot{\mathbf{x}}_s, \mathbf{x}_a, \mathbf{u}$, respectively. The derivatives $\mathbf{K}_{ss}(\psi) = -\frac{\partial \mathbf{h}}{\partial \mathbf{x}_s}(\psi)$, $\mathbf{D}_s(\psi) = -\frac{\partial \mathbf{h}}{\partial \dot{\mathbf{x}}_s}(\psi)$, $\mathbf{K}_{sa}(\psi) = -\frac{\partial \mathbf{h}}{\partial \mathbf{x}_a}(\psi)$, and $\mathbf{G}_s(\psi) = \frac{\partial \mathbf{h}}{\partial \mathbf{u}}(\psi)$ are matrix functions dependent on the azimuthal angle ψ and are calculated at a finite number of azimuthal steps (in the current study, 320 equally spaced steps are used in a revolution) using a central differencing scheme given as

$$\frac{\partial \mathbf{h}}{\partial \mathbf{x}_s} \approx \frac{\mathbf{h}(\bar{\mathbf{x}}_s + \Delta\mathbf{x}_s, \dot{\bar{\mathbf{x}}}_s, \bar{\mathbf{x}}_a, \bar{\mathbf{u}}) - \mathbf{h}(\bar{\mathbf{x}}_s - \Delta\mathbf{x}_s, \dot{\bar{\mathbf{x}}}_s, \bar{\mathbf{x}}_a, \bar{\mathbf{u}})}{2\Delta\mathbf{x}_s} \tag{14}$$

$$\frac{\partial \mathbf{h}}{\partial \dot{\mathbf{x}}_s} \approx \frac{\mathbf{h}(\bar{\mathbf{x}}_s, \dot{\bar{\mathbf{x}}}_s + \Delta\dot{\mathbf{x}}_s, \bar{\mathbf{x}}_a, \bar{\mathbf{u}}) - \mathbf{h}(\bar{\mathbf{x}}_s, \dot{\bar{\mathbf{x}}}_s - \Delta\dot{\mathbf{x}}_s, \bar{\mathbf{x}}_a, \bar{\mathbf{u}})}{2\Delta\dot{\mathbf{x}}_s} \tag{15}$$

$$\frac{\partial \mathbf{h}}{\partial \mathbf{x}_a} \approx \frac{\mathbf{h}(\bar{\mathbf{x}}_s, \dot{\bar{\mathbf{x}}}_s, \bar{\mathbf{x}}_a + \Delta\mathbf{x}_a, \bar{\mathbf{u}}) - \mathbf{h}(\bar{\mathbf{x}}_s, \dot{\bar{\mathbf{x}}}_s, \bar{\mathbf{x}}_a - \Delta\mathbf{x}_a, \bar{\mathbf{u}})}{2\Delta\mathbf{x}_a} \tag{16}$$

$$\frac{\partial \mathbf{h}}{\partial \mathbf{u}} \approx \frac{\mathbf{h}(\bar{\mathbf{x}}_s, \dot{\bar{\mathbf{x}}}_s, \bar{\mathbf{x}}_a, \bar{\mathbf{u}} + \Delta\mathbf{u}) - \mathbf{h}(\bar{\mathbf{x}}_s, \dot{\bar{\mathbf{x}}}_s, \bar{\mathbf{x}}_a, \bar{\mathbf{u}} - \Delta\mathbf{u})}{2\Delta\mathbf{u}} \tag{17}$$

where $(\bar{\mathbf{x}}_s, \dot{\bar{\mathbf{x}}}_s, \bar{\mathbf{x}}_a, \bar{\mathbf{u}})$ represents a periodic eqilibrium condition.

The differential equations corresponding to the RFA aerodynamic model in the AVINOR code can be represented as

$$\dot{\mathbf{x}}_a = \mathbf{h}_a(\mathbf{x}_s, \dot{\mathbf{x}}_s, \mathbf{x}_a, \mathbf{u}). \tag{18}$$

Linearization about a periodic equilibrium yields

$$\begin{aligned}\Delta\dot{\mathbf{x}}_a =& \frac{\partial \mathbf{h}_a}{\partial \mathbf{x}_s}(\psi)\Delta\mathbf{x}_s + \frac{\partial \mathbf{h}_a}{\partial \dot{\mathbf{x}}_s}(\psi)\Delta\dot{\mathbf{x}}_s + \frac{\partial \mathbf{h}_a}{\partial \mathbf{x}_a}(\psi)\Delta\mathbf{x}_a \\ &+ \frac{\partial \mathbf{h}_a}{\partial \mathbf{u}}(\psi)\Delta\mathbf{u},\end{aligned} \tag{19}$$

or

$$\begin{aligned}\Delta\dot{\mathbf{x}}_a = &-\mathbf{K}_{as}(\psi)\Delta\mathbf{x}_s - \mathbf{K}_{aa}(\psi)\Delta\mathbf{x}_a - \mathbf{D}_a(\psi)\Delta\dot{\mathbf{x}}_s \\ &+ \mathbf{G}_a(\psi)\Delta\mathbf{u},\end{aligned} \tag{20}$$

where the derivatives $\mathbf{K}_{as}(\psi) = -\frac{\partial \mathbf{h}_a}{\partial \mathbf{x}_s}(\psi)$, $\mathbf{D}_a(\psi) = -\frac{\partial \mathbf{h}_a}{\partial \dot{\mathbf{x}}_s}(\psi)$, $\mathbf{K}_{aa}(\psi) = -\frac{\partial \mathbf{h}_a}{\partial \mathbf{x}_a}(\psi)$, and $\mathbf{G}_a(\psi) = \frac{\partial \mathbf{h}_a}{\partial \mathbf{u}}(\psi)$ represent the effect of perturbations in the various state variables and control inputs on the aerodynamic state derivatives. A similar linearization procedure is adopted for the output equation. In this study the vibratory hub loads are chosen as the output quantities. The vibratory hub shears and moments are obtained from the integration of the distributed inertial and aerodynamic loads over the entire blade span. This relation can be represented by a nonlinear function as

$$\mathbf{y} = \mathbf{f}(\mathbf{x}_s, \dot{\mathbf{x}}_s, \mathbf{x}_a, \mathbf{u}), \tag{21}$$

and is linearized about a periodic equilibrium. The

linearized equation is expressed as

(22)
$$\Delta\mathbf{y} = \frac{\partial\mathbf{f}}{\partial\mathbf{x}_s}(\psi)\Delta\mathbf{x}_s + \frac{\partial\mathbf{f}}{\partial\dot{\mathbf{x}}_s}(\psi)\Delta\dot{\mathbf{x}}_s + \frac{\partial\mathbf{f}}{\partial\mathbf{x}_a}(\psi)\Delta\mathbf{x}_a + \frac{\partial\mathbf{f}}{\partial\mathbf{u}}(\psi)\Delta\mathbf{u},$$

or

(23)
$$\Delta\mathbf{y} = \mathbf{P}_s(\psi)\Delta\mathbf{x}_s + \mathbf{Q}(\psi)\Delta\dot{\mathbf{x}}_s + \mathbf{P}_a(\psi)\Delta\mathbf{x}_a + \mathbf{R}(\psi)\Delta\mathbf{u}.$$

The partial derivatives $\mathbf{P}_s(\psi) = \frac{\partial\mathbf{f}}{\partial\mathbf{x}_s}(\psi)$, $\mathbf{P}_a(\psi) = \frac{\partial\mathbf{f}}{\partial\mathbf{x}_a}(\psi)$, $\mathbf{Q}(\psi) = \frac{\partial\mathbf{f}}{\partial\dot{\mathbf{x}}_s}(\psi)$, and $\mathbf{R}(\psi) = \frac{\partial\mathbf{f}}{\partial\mathbf{u}}(\psi)$ represent the change in the vibratory loads due to a unit perturbation in the state variables, their derivatives, and the control inputs, respectively. The central differencing scheme is used to evaluate all the partial derivatives in this study. The final LTP representation of the helicopter model can be expressed in a state space form as follows:

(24)
$$\dot{\xi} = \mathbf{A}(\psi)\xi + \mathbf{B}(\psi)\upsilon$$

(25)
$$\zeta = \mathbf{C}(\psi)\xi + \mathbf{E}(\psi)\upsilon$$

where

$$\xi = [\Delta\mathbf{x}_s \quad \Delta\mathbf{x}_a \quad \Delta\dot{\mathbf{x}}_s]^T,$$
$$\upsilon = [\Delta\mathbf{u}]^T,$$
$$\zeta = [\Delta\mathbf{y}]^T,$$
$$\mathbf{A}(\psi) = \begin{bmatrix} \mathbf{0} & \mathbf{0} & \mathbf{I} \\ -\mathbf{K}_{as}(\psi) & -\mathbf{K}_{aa}(\psi) & -\mathbf{D}_a(\psi) \\ -\mathbf{K}_{ss}(\psi) & -\mathbf{K}_{sa}(\psi) & -\mathbf{D}(\psi) \end{bmatrix},$$
$$\mathbf{B}(\psi) = \begin{bmatrix} \mathbf{0} \\ \mathbf{G}_a(\psi) \\ \mathbf{G}_s(\psi) \end{bmatrix},$$
$$\mathbf{C}(\psi) = [\mathbf{P}_s(\psi) \quad \mathbf{P}_a(\psi) \quad \mathbf{Q}(\psi)],$$
$$\mathbf{E}(\psi) = [\mathbf{R}(\psi)].$$

Linearized models extracted in this study will be used to examine interactions between on-blade control and the flight control systems. In order to study coupled rotor-fuselage dynamics of a helicopter, it is convenient to describe the rotating blade motion in a non-rotating coordinate system. Multiblade coordinates (MBC) are widely used in the literature to express the blade motion in the non-rotating coordinate system [15]. The blade equations of motion in AVINOR are solved in the rotating frame using rotating blade coordinates (RBC). Therefore, when extracting the linearized models from AVINOR, a coordinate transformation is used to transform the blade degrees of freedom from RBC to MBC. For a 4-bladed rotor, the MBC can be expressed in terms of the rotating blade coordinates as follows:

(26)
$$x_{m0} = \frac{1}{4}\sum_{n=1}^{4} x_n$$

(27)
$$x_{m1c} = \frac{1}{2}\sum_{n=1}^{4} x_n \cos\psi_n$$

(28)
$$x_{m1s} = \frac{1}{2}\sum_{n=1}^{4} x_n \sin\psi_n$$

(29)
$$x_{m2} = \frac{1}{4}\sum_{n=1}^{4} (-1)^n x_n$$

where $x_{m0}, x_{m1c}, x_{m1s}, x_{m2}$ are the collective, cosine, sine, and differential multi-blade coordinates, x_n and ψ_n are the individual blade coordinate and azimuth angle corresponding to the n^{th} blade, respectively. For a 4-bladed rotor, the individual blade coordinate of the nth blade is given in terms of MBC as:

(30)
$$x_n = x_{m0} + x_{m1c}\cos\psi_n + x_{m1s}\sin\psi_n + (-1)^n x_{m2}.$$

Similar transformations are defined for the control inputs. The use of these transformations to derive a linearized helicopter system of equations in terms of MBC is provided in Ref. 5.

The FEMR approach [9] is used to extract LTI models from the LTP models (Eqs. (24), (25)). This approach is based on a Fourier approximation to the state, output and input variables $\Delta\mathbf{x}_s$, $\Delta\mathbf{x}_a$, $\Delta\mathbf{u}$, and $\Delta\mathbf{y}$, given as:

(31)
$$\Delta\mathbf{x}_s = \Delta\mathbf{x}_s^0 + \sum_{n=1}^{N}[\Delta\mathbf{x}_s^{nc}\cos(n\psi) + \Delta\mathbf{x}_s^{ns}\sin(n\psi)],$$

(32)
$$\Delta\mathbf{x}_a = \Delta\mathbf{x}_a^0 + \sum_{n=1}^{N}[\Delta\mathbf{x}_a^{nc}\cos(n\psi) + \Delta\mathbf{x}_a^{ns}\sin(n\psi)],$$

(33)
$$\Delta\mathbf{u} = \Delta\mathbf{u}^0 + \sum_{m=1}^{M}[\Delta\mathbf{u}^{mc}\cos(m\psi) + \Delta\mathbf{u}^{ms}\sin(m\psi)],$$

(34)
$$\Delta\mathbf{y} = \Delta\mathbf{y}^0 + \sum_{l=1}^{L}[\Delta\mathbf{y}^{lc}\cos(n\psi) + \Delta\mathbf{y}^{ls}\sin(l\psi)].$$

where $\Delta\mathbf{x}_s^0, \Delta\mathbf{x}_a^0, \Delta\mathbf{u}_0, \Delta\mathbf{y}_0$ are the average components, $\Delta\mathbf{x}_s^{nc}, \Delta\mathbf{x}_a^{nc}, \Delta\mathbf{u}^{mc}, \Delta\mathbf{y}^{lc}$ are the cosine harmonic components, and $\Delta\mathbf{x}_s^{ns}, \Delta\mathbf{x}_a^{ns}, \Delta\mathbf{u}^{ms}, \Delta\mathbf{y}^{ls}$ are the sine harmonic components. Differentiating the expansion for $\Delta\mathbf{x}_s$ and $\Delta\mathbf{x}_a$ with respect to ψ,

(35)
$$\Delta\dot{\mathbf{x}}_s = \Delta\dot{\mathbf{x}}_s^0 + \sum_{n=1}^{N}[(\Delta\dot{\mathbf{x}}_s^{nc} + n\Delta\mathbf{x}_s^{ns})\cos(n\psi) + (\Delta\dot{\mathbf{x}}_s^{ns} - n\Delta\mathbf{x}_s^{nc})\sin(n\psi)],$$

(36)
$$\Delta\dot{\mathbf{x}}_a = \Delta\dot{\mathbf{x}}_a^0 + \sum_{n=1}^{N}[(\Delta\dot{\mathbf{x}}_a^{nc} + n\Delta\mathbf{x}_a^{ns})\cos(n\psi) + (\Delta\dot{\mathbf{x}}_a^{ns} - n\Delta\mathbf{x}_a^{nc})\sin(n\psi)].$$

Differentiating the structural equation again yields

(37)
$$\Delta\ddot{\mathbf{x}}_s = \Delta\ddot{\mathbf{x}}_s^0 + \sum_{n=1}^{N}[(\Delta\ddot{\mathbf{x}}_s^{nc} + 2n\Delta\dot{\mathbf{x}}_s^{ns} - n^2\Delta\mathbf{x}_s^{nc})\cos(n\psi) + (\Delta\ddot{\mathbf{x}}_s^{ns} - 2n\Delta\dot{\mathbf{x}}_s^{nc} - n^2\Delta\mathbf{x}_s^{ns})\sin(n\psi)].$$

Fourier expansions are also defined for the system matrices, for example,

(38)
$$\mathbf{K}_{ss}(\psi) = \mathbf{K}_{ss}^0 + \sum_{n=1}^{N}[\mathbf{K}_{ss}^{nc}\cos(n\psi) + \mathbf{K}_{ss}^{ns}\sin(n\psi)],$$

where

$$\mathbf{K}_{ss}^0 = \frac{1}{2\pi}\int_0^{2\pi}\mathbf{K}_{ss}(\psi)d\psi,$$
$$\mathbf{K}_{ss}^{ic} = \frac{1}{\pi}\int_0^{2\pi}\mathbf{K}_{ss}(\psi)\cos(i\psi)d\psi,$$
$$\mathbf{K}_{ss}^{is} = \frac{1}{\pi}\int_0^{2\pi}\mathbf{K}_{ss}(\psi)\sin(i\psi)d\psi.$$
$$i = 1, 2, \ldots, N$$

Substituting Eqs. (31)-(33), (35), and (37) into the blade structural equation of motion, Eq. (13) yields,

(39)
$$\begin{aligned}
&\Delta\ddot{\mathbf{x}}_s^0 + \sum_{i=1}^{N}[(\Delta\ddot{\mathbf{x}}_s^{ic} + 2i\Delta\dot{\mathbf{x}}_s^{is} - i^2\Delta\mathbf{x}_s^{ic})\cos(i\psi) \\
&\qquad + (\Delta\ddot{\mathbf{x}}_s^{is} - 2i\Delta\dot{\mathbf{x}}_s^{ic} - i^2\Delta\mathbf{x}_s^{is})\sin(i\psi)] \\
&= -\mathbf{K}_{ss}(\psi)\left\{\Delta\mathbf{x}_s^0 + \sum_{n=1}^{N}[\Delta\mathbf{x}_s^{nc}\cos(n\psi) + \Delta\mathbf{x}_s^{ns}\sin(n\psi)]\right\} \\
&- \mathbf{K}_{sa}(\psi)\left\{\Delta\mathbf{x}_a^0 + \sum_{n=1}^{N}[\Delta\mathbf{x}_a^{nc}\cos(n\psi) + \Delta\mathbf{x}_a^{ns}\sin(n\psi)]\right\} \\
&- \mathbf{D}_s(\psi)\left\{\Delta\dot{\mathbf{x}}_s^0 + \sum_{n=1}^{N}[(\Delta\dot{\mathbf{x}}_s^{nc} + n\Delta\mathbf{x}_s^{ns})\cos(n\psi) + (\Delta\dot{\mathbf{x}}_s^{ns} - n\Delta\mathbf{x}_s^{nc})\sin(n\psi)]\right\} \\
&+ \mathbf{G}_s(\psi)\left\{\Delta\mathbf{u}^0 + \sum_{m=1}^{M}[\Delta\mathbf{u}^{mc}\cos(m\psi) + \Delta\mathbf{u}^{ms}\sin(m\psi)]\right\}
\end{aligned}$$

Equation for the average component $\mathbf{x}_s^0$ is obtained by applying $\frac{1}{2\pi}\int_0^{2\pi}$ averaging procedure on both sides of Eq. (39). Equation for the i^{th} harmonic cosine component $\Delta\mathbf{x}_s^{ic}$ can be obtained by multiplying both sides of Eq. (39) by $\frac{1}{\pi}\cos(i\psi)$ and integrating it over one revolution. In a similar manner, the equation for the i^{th} harmonic sine component $\Delta\mathbf{x}_s^{is}$ can be obtained by multiplying both sides of Eq. (39) by $\frac{1}{\pi}\sin(i\psi)$ and integrating it over one revolution. Performing similar operations on the aerodynamic state equation and the output equation, and defining augmented state, input, and output vectors as

$$\begin{aligned}
\mathbf{x}_{\text{aug}} &= [\mathbf{x}_s^0 \ldots \mathbf{x}_s^{nc} \quad \mathbf{x}_s^{ns} \ldots \dot{\mathbf{x}}_s^0 \ldots \dot{\mathbf{x}}_s^{nc} \quad \dot{\mathbf{x}}_s^{ns} \ldots \\
&\qquad \ldots \mathbf{x}_a^0 \ldots \mathbf{x}_a^{nc} \quad \mathbf{x}_a^{ns} \ldots]^T, \\
\mathbf{u}_{\text{aug}} &= [\mathbf{u}^0 \ldots \mathbf{u}^{mc} \quad \mathbf{u}^{ms} \ldots]^T, \\
\mathbf{y}_{\text{aug}} &= [\mathbf{y}^0 \ldots \mathbf{y}^{lc} \quad \mathbf{y}^{ls} \ldots]^T,
\end{aligned}$$

the linear equations can be consolidated and expressed as a state-space LTI model given by

(40)
$$\dot{\mathbf{x}}_{\text{aug}} = \begin{bmatrix} \mathbf{0} & \mathbf{0} & \mathbf{I} \\ \mathbf{A}_{21} & \mathbf{A}_{22} & \mathbf{A}_{23} \\ \mathbf{A}_{31} & \mathbf{A}_{32} & \mathbf{A}_{33} \end{bmatrix}\mathbf{x}_{\text{aug}} + \begin{bmatrix} \mathbf{0} \\ \mathbf{B}_2 \\ \mathbf{B}_3 \end{bmatrix}\mathbf{u}_{\text{aug}},$$

(41)
$$\mathbf{y}_{\text{aug}} = [\mathbf{C}_1 \quad \mathbf{C}_2 \quad \mathbf{C}_3]\,\mathbf{x}_{\text{aug}} + \mathbf{E}_1\mathbf{u}_{\text{aug}},$$

where the matrices $\mathbf{A}_{21}$, $\mathbf{A}_{22}$, $\mathbf{A}_{23}$, $\mathbf{A}_{31}$, $\mathbf{A}_{32}$, $\mathbf{A}_{33}$, $\mathbf{B}_2$, $\mathbf{B}_3$, $\mathbf{C}_1$, $\mathbf{C}_2$, $\mathbf{C}_3$, and $\mathbf{E}_1$ are defined in Ref. 5.

4 Closed-loop Control Using LTI Models

On-blade control devices are implemented in closed-loop mode for rotorcraft vibration and noise reduction. A schematic of closed-loop control using the HHC controller is shown in Fig. 1. Therefore, to accurately study on-blade control and flight control interactions, it is imperative that the LTI models retain the closed-loop characteristics of the nonlinear model. In order to evaluate the closed-loop fidelity of the LTI models, extracted using the procedure described in the previous section, closed-loop performance of the on-blade control devices predicted using the LTI models is compared to that predicted using the nonlinear model. Specifically, the optimal flap deflection predictions and the reduction in vibratory hub loads are compared. An illustration of on-blade vibration control with the LTI helicopter model and the HHC controller implemented in a feedback loop is shown in Fig. 3. The LTI models predict only perturbations in the vibratory hub loads due to flap deflection. Therefore, the steady state hub loads are added to the LTI model predictions to obtain the complete vibratory loads. Then, a Fourier transform is used to extract the 4/rev components of the vibratory loads, which in turn are fed into the higher harmonic controller. The classical HHC controller is used to determine the optimal control input for vibratory load reduction. An adaptive version of the algorithm is not necessary when working with LTI helicopter models. The control input is a combination of the 2/rev, 3/rev, 4/rev, and 5/rev harmonic components of the flap deflection. The sensitivity matrix $\mathbf{T}$, used in the HHC algorithm, is also obtained using the LTI model. A comparison of the $\mathbf{T}$ matrices obtained from the nonlinear and the LTI models revealed negligible differences. This can be attributed to the fact that small flap deflection perturbation values were used to obtain the $\mathbf{T}$ matrices.

5 Implementation, Verification, and Discussion

The rotor configuration considered is a four-bladed hingeless rotor, resembling the BO-105 type rotor; the rotor parameters are listed in Table 1. All the values in the table (except C_W, γ, and σ) have been nondimensionalized using M_b, L_b, and $1/\Omega$ for mass, length and time, respectively. The mass and stiffness distributions are assumed to be constant along the span of the blade. The rotor is trimmed using a propulsive trim procedure. All the blades are assumed to be identical.

Table 1: Rotor configuration parameters used.

Dimensional Rotor Data	
$R = 4.91$ m	
$M_b = 27.35$ kg	
$\Omega = 425$ RPM	
Nondimensional Rotor Data	
$N_b = 4$	$L_b = 1.0$
$c/R = 0.05498$	$\theta_{\text{tw}} = -8°$
$e = 0$	
$X_A = 0$	$X_{Ib} = 0$
$\omega_F = 1.124, 3.40, 7.60$	$\omega_L = 0.732, 4.458$
$\omega_T = 3.17, 9.08$	
$\gamma = 5.5$	$\sigma = 0.07$
$\beta_p = 2.5°$	
Helicopter Data	
$C_W = 0.005$	$fC_{df} = 0.031$
$X_{FA} = 0.0$	$Z_{FA} = 0.3$
$X_{FC} = 0.0$	$Z_{FC} = 0.3$

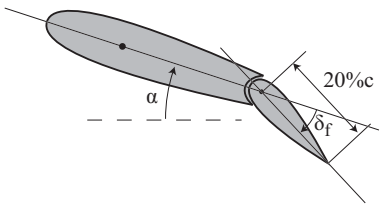

Figure 4: A 20%c conventional plain flap configuration.

Linearized time-periodic and time-invariant models were extracted from the AVINOR code at two different flight conditions, namely, a steady descending flight condition with advance ratio $\mu = 0.15$ and descent angle $\alpha_{\text{D}} = 6.5°$, which represents heavy BVI conditions and a cruise flight condition with advance ratio $\mu = 0.30$. A single plain flap with a 20% chord length, shown in Fig. 4, is used as the active control device. The flap is centered at 75% span location and its spanwise length is 12% of the blade radius as shown in Fig. 5. The LTP model is based on 7 states corresponding to the blade structural degrees of freedom (3 flap, 2 lead-lag, and 2 torsional), 7 states corresponding to their derivatives, and 100 states corresponding to the RFA aerodynamic model states. This is equivalent to 456

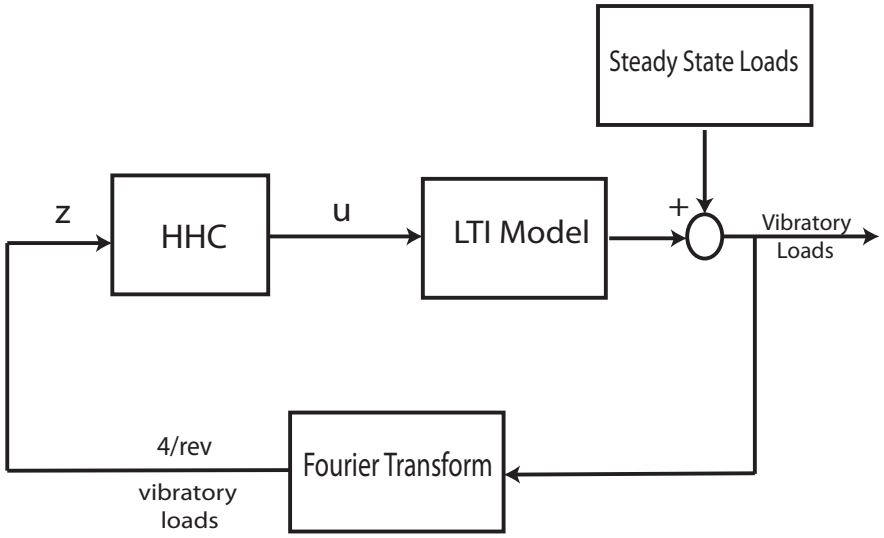

Figure 3: An illustration of closed-loop on-blade vibration control using a LTI helicopter model and the HHC controller.

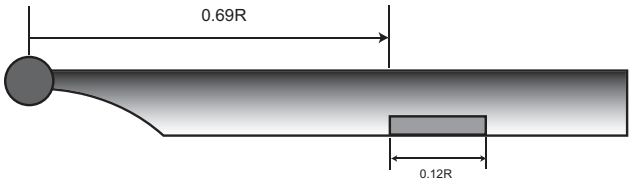

Figure 5: Spanwise configuration of the 20%c plain flap on the rotor blade.

(114*4) states when expressed using the multi-blade coordinates. The AVINOR code does not account for the body degrees of freedom. In order to study the effect of active vibration control devices on the flight handling qualities, the body degrees of freedom have to be embedded into linear models, however, this issue will be addressed in future studies. A rotor revolution is divided into 320 azimuthal steps in order to calculate the LTP model matrices $A(\psi), B(\psi), C(\psi)$, and $E(\psi)$. A trial and error procedure was used to determine the optimum perturbation values. A 10% perturbation is used for the structural and aerodynamic states and a 0.25° perturbation is used for the flap deflection in LTP model extraction. The flap deflection control input in the AVINOR code is specified in the frequency domain through the harmonic component amplitudes. In order to specify a constant perturbation in flap deflection, during LTP model extraction, the cosine 0/rev component is set to 0.25° and all the other components are set to 0. Thus, the effects of flap deflection rate ($\dot{u}$) are neglected. The LTI model is based on the first 4 harmonic components in the Fourier expansion. The linearized models were verified in Ref. 5 by comparing their output response with the nonlinear model response corresponding to a *open-loop* higher harmonic flap deflection. The current study verifies the *closed-loop* fidelity of the LTI models when used for vibratory hub load reduction.

In order to assess its closed-loop fidelity, the LTI model extracted at the low-speed descending flight condition is implemented in the control loop shown in Fig. 3. Initially, the control sensitivity matrix used by the HHC controller is computed. Subsequently, the controller is engaged in closed-loop with the LTI model. The optimal flap deflections for vibration reduction predicted by the HHC controller when used in conjunction with the LTI and the nonlinear models are compared in Fig. 6(a). The flap deflection is comprised of the 2/rev, 3/rev, 4/rev, and 5/rev harmonic components and the amplitude is limited to 1°. The flap deflection is limited to account for actuator saturation using the algorithm described in Ref.16. This limit on the flap deflection is refered to as the saturation limit. The LTI and nonlinear model based predictions agree reasonably well, especially in the magnitude and the azimuthal locations of the peaks and troughs. The differences in the two predictions can be quantified by a root mean square (RMS) error term defined as $E = \sqrt{(\Delta\delta_{2c}^2 + \Delta\delta_{2s}^2 + ... + \Delta\delta_{5c}^2 + \Delta\delta_{5s}^2)/8}$. The RMS error for the flap deflections in Fig. 6(a) is 0.0022. The corresponding vibratory hub loads are

compared to the baseline loads in Fig. 6(b). Performance of the controller is evaluated based on the reduction achieved in the vibratory cost function $J = F_{HX4}^2 + F_{HY4}^2 + F_{HZ4}^2 + M_{HX4}^2 + M_{HY4}^2 + M_{HZ4}^2$. The nonlinear model yields a 24% reduction in the cost function compared to 34% obtained by the LTI model.

Similar comparisons are performed with the maximum flap deflection set to 2°. The optimal flap deflections predicted by the LTI and the nonlinear models are compared in Fig. 7(a). The LTI and nonlinear model based predictions agree reasonably well. There is good agreement in the magnitude of the peaks and troughs. However, their azimuthal locations show slightly bigger errors. The RMS error for the flap deflections in Fig. 7(a) is 0.0063. The corresponding vibratory hub loads are compared to the baseline loads in Fig. 7(b). The nonlinear model yields a 40% reduction in the cost function compared to 65% obtained by the LTI model. Results were also generated for a maximum flap deflection of 4°. The optimal flap deflections are compared in Fig. 8(a). The trends are similar to those observed for a 2° limit. However, the RMS error is much higher at 0.0134. Thus, the error in flap deflection predictions is increasing steadily with an increasing saturation limit. This is because as the flap deflection limit is increased, the dynamics are swayed further away from the operating condition and the small perturbation assumption is violated. The corresponding vibratory hub loads are compared to the baseline loads in Fig. 8(b). The nonlinear model yields a 85% reduction in the cost function compared to 92% obtained by the LTI model.

Linearized models were also extracted at a cruise flight condition with $\mu = 0.30$. A closed-loop fidelity assessment was carried out by comparing the LTI and nonlinear model closed-loop vibration reduction performance. The optimal flap deflections predicted by the HHC controller in conjunction with the linear and nonlinear models are compared in Fig. 9(a). The flap deflection amplitude is restricted to 2°. The trends are similar to those observed in the case of low advance ratio flight showing good agreement in the magnitudes of the peaks and troughs. The RMS error between the flap deflections shown in Fig. 9(a) is 0.0075. The corresponding vibratory hub loads are compared in Fig. 9(b). The nonlinear model yields a 90% reduction in the vibratory cost function J whereas the LTI model yields 82% reduction. Therefore, closed-loop performance of the nonlinear and the LTI models compare reasonably well even at a high-speed flight condition.

The LTI models extracted at the cruise condition were also compared to the nonlinear model with flap deflection restricted to less than 4°. The flap deflections from the linear and nonlinear models are compared in Fig. 10(a). The RMS error between the two deflection histories is 0.0158, which is twice as large compared to the 2° limit case. The corresponding vibratory hub loads are compared in Fig. 10(b). The reduction achieved by the linear and nonlinear models is similar in all but the longitudinal hub shear. The LTI model yields 86% reduction in the overall vibratory cost function whereas the nonlinear model shows 95% reduction.

6 Conclusions

Linearized time-periodic models that can predict the effects of on-blade trailing-edge flaps were extracted from a high-fidelity nonlinear helicopter model. The time-periodic models were in turn used to extract linearized time-invariant models using a Fourier expansion based model reduction method. These linearized models are intended for studies examining the interaction between on-blade control and the primary flight control system. On-blade control is usually implemented in closed-loop mode, therefore, the LTI models were verified for closed-loop performance fidelity. The higher harmonic controller was used with the 2/rev-5/rev harmonic components of the flap deflection as the control input and vibratory hub loads as the output. Closed-loop performance of the LTI model is compared to that of the nonlinear model at a low-speed descending flight and a cruise flight condition. The principal conclusions are:

1. For a low-speed descending flight, the flap deflection predictions based on the LTI and nonlinear models agree well, in both magnitude and azimuthal locations of the peaks and troughs. For a 1° saturation limit on the flap deflection, the RMS error between the flap deflections is 0.0022. A comparison of the corresponding vibratory hub loads indicates that the nonlinear model yields a 24% reduction in the vibratory cost function compared to 34% obtained with the LTI model.

2. Increasing the flap deflection saturation limit to 2° increases the RMS error between the linear and nonlinear model flap deflections to 0.0063. The agreement between the flap deflections is reasonably good. The nonlinear

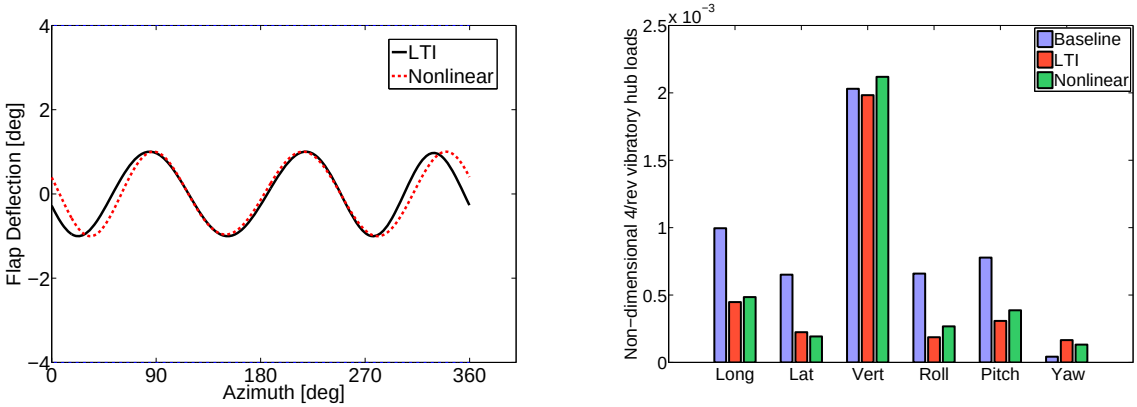

(a) Flap deflection

(b) Vibratory loads

Figure 6: Verification of the closed-loop flap deflection and vibratory loads obtained from the LTI and nonlinear models with saturation limit 1°. $\mu = 0.15$, $\alpha_{\text{D}} = 6.5°$.

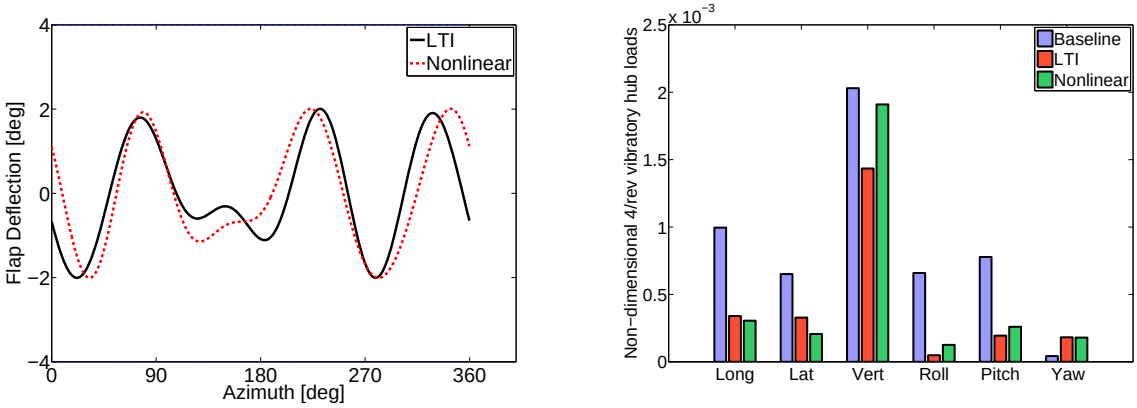

(a) Flap deflection

(b) Vibratory loads

Figure 7: Verification of the closed-loop flap deflection and vibratory loads obtained from the LTI and nonlinear models with saturation limit 2°. $\mu = 0.15$, $\alpha_{\text{D}} = 6.5°$.

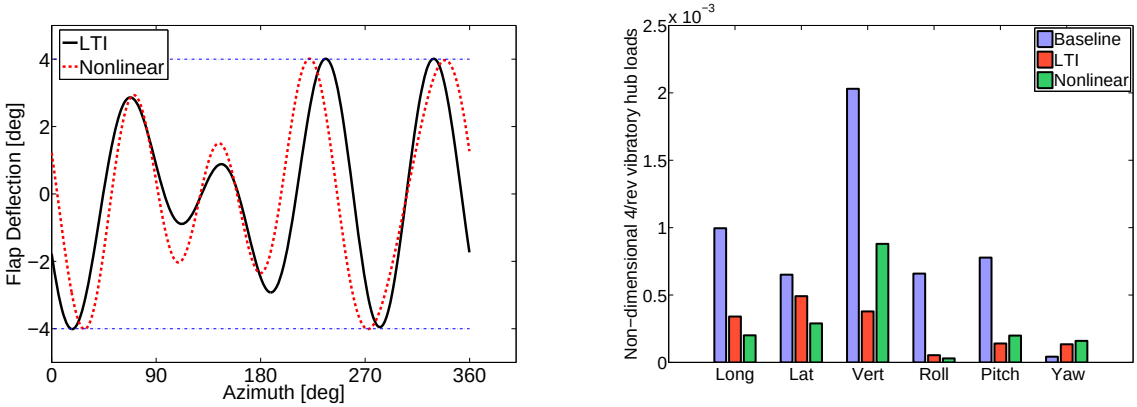

(a) Flap deflection

(b) Vibratory loads

Figure 8: Verification of the closed-loop flap deflection and vibratory loads obtained from the LTI and nonlinear models with saturation limit 4°. $\mu = 0.15$, $\alpha_{\text{D}} = 6.5°$.

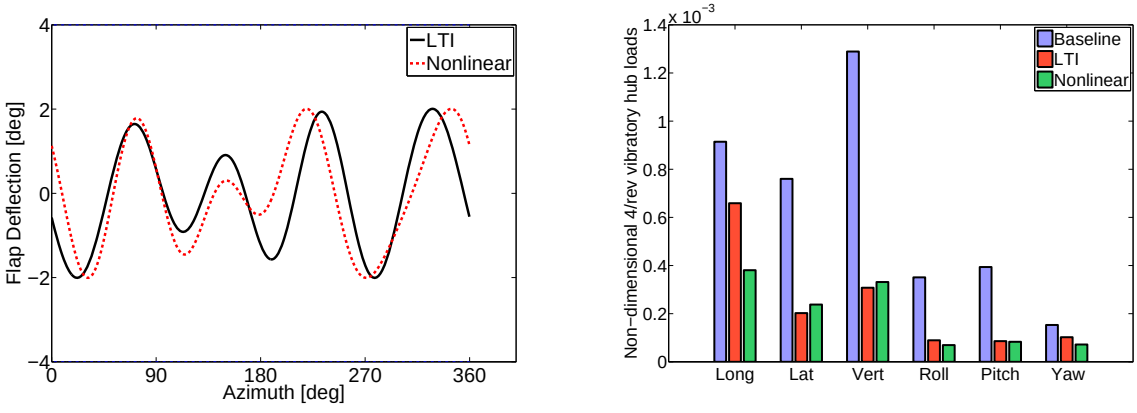

(a) Flap deflection

(b) Vibratory loads

Figure 9: Verification of the closed-loop flap deflection and vibratory loads obtained from the LTI and nonlinear models with saturation limit 2°. $\mu = 0.30$.

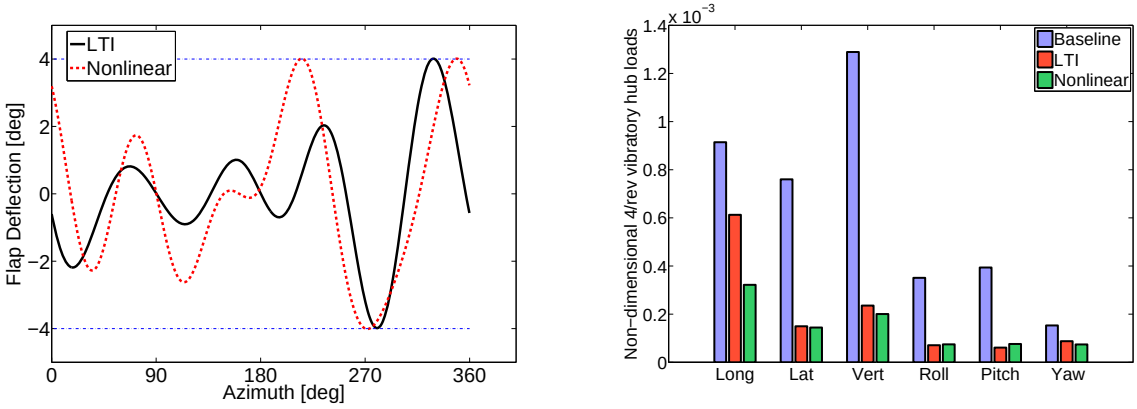

(a) Flap deflection

(b) Vibratory loads

Figure 10: Verification of the closed-loop flap deflection and vibratory loads obtained from the LTI and nonlinear models with saturation limit 4°. $\mu = 0.30$.

model yields a 40% reduction in the cost function compared to 65% obtained with the LTI model. Thus, the linear model overpredicts the vibration reduction performance.

3. Increasing the flap deflection limit, at low-speed, to 4° increases the RMS error in flap deflections to 0.0134. Thus, the error in flap deflection predictions increases steadily with increasing saturation limits. This is because, as the flap deflection limit is increased, the dynamics are forced further away from the operating condition and the small perturbation assumption is violated. The nonlinear and linearized models yield 85% and 92% reduction in the vibratory cost function, respectively.

4. Similar comparisons were performed at a cruise condition, $\mu = 0.3$, with the flap deflection saturation limit set to 2°. The linear and nonlinear model predictions agree reasonably well. The RMS error between the flap deflections is 0.0075. The nonlinear model yields a 90% reduction in the vibratory cost function whereas the LTI model yields 82% reduction.

5. At cruise condition, with the flap deflection limit set to 4°, the RMS error between the flap deflections is 0.0158. This represents approximately a 100% increase with a 2° increase in the saturation limit. This is similar to the trends noted in the low-speed case. In this case, the LTI model yields a 86% reduction in the vibratory cost function whereas the nonlinear model yields 95% reduction.

Acknowledgments

This research was supported by the Vertical Lift Research Center of Excellence (VLRCOE) sponsored by NRTC and U.S. Army with Dr. M. J. Bhagwat as the grant monitor.

REFERENCES

1. Patt, D. , Liu, L. , and Friedmann, P. P. , "Simultaneous Vibration and Noise Reduction in Rotorcraft Using Aeroelastic Simulation," Journal of the American Helicopter Society, Vol. 51, (2), April 2006, pp. 127–140.

2. Rabourdin, A. , Maurice, J. B. , Dieterich, O. , and Konstanzer, P. , "Blue Pulse Active Rotor Control at Airbus Helicopters - New EC145 Demonstrator and Flight Test Results," Proceedings of the 70th American Helicopter Society Annual Forum, Montreal, Canada, May 2014.

3. Straub, F. K. , Anand, V. , Birchette, T. S. , and Lau, B. H. , "Wind Tunnel Test of the SMART Active Flap Rotor," Proceedings of the 65th American Helicopter Society Annual Forum, Grapevine,TX, May 2009.

4. Padthe, A. K. , Liu, L. , and Friedmann, P. P. , "Numerical Evaluation of Microflaps for On Blade Control of Noise and Vibration," Proceedings of the 52nd AIAA/ASME/ASCE/AHS/ACS Structures, Structural Dynamics and Materials Conference, Denver, CO, April 2011.

5. Padthe, A. K. , Friedmann, P. P. , and Prasad, J. V. R. , "High Fidelity Linear Time-Invariant Models for Rotor and Flight Control Interaction Studies," Proceedings of the 5th Decennial AHS Aeromechanics Specialists' Conference, San Francisco, CA, Jan 2014.

6. Anon., "Handling Qualities Requirements for Military Rotorcraft," Aeronautical Design Standard-33 (ADS-33E-PRF), US Army Aviation and Missile Command, 2000.

7. Colaneri, P. , Celi, R. , and Bittanti, S. , "Constant-coefficient Representations of Periodic Coefficient Discrete Linear Systems," Proceedings of the AHS 4th Decennial Specialist's Conference on Aeromechanics, San Francisco, CA, Jan 2004.

8. Cheng, R. P. , Tischler, M. B. , and Celi, R. , "A High-Order, Time Invariant, Linearized Model for Application to HHC/AFCS Interaction Studies," Proceedings of the 59th Annual Forum of the American Helicopter Society, Phoenix, AZ, May 2003.

9. Prasad, J. V. R. , Olcer, F. E. , Sankar, L. N. , and He, C. , "Linear Time Invariant Models for Integrated Flight and Rotor Control," Proceedings of the 35th European Rotorcraft Forum, Hamburg, Germany, September 2009.

10. Lopez, M. and Prasad, J. V. R. , "Fidelity of Reduced-Order Time-Invariant Linear (LTI) Models for Integrated Flight and Rotor Control Applications," Proceedings of the 69th Annual Forum of the American Helicopter Society, Phoenix, AZ, May 2013.

11. Abraham, M. D. , Olcer, F. E. , Costello, M. F. , Takahashi, M. D. , and Tischler, M. B. , "Integrated Design of AFCS and HHC for Rotorcraft Vibration Reduction Using Dynamic Crossfeeds," Proceedings of the 67th Annual Forum of the American Helicopter Society, Virginia Beach, VA, May 2011.

12. Glaz, B. , Friedmann, P. P. , Liu, L. , Kumar, D. , and Cesnik, C. E. S. , "The AVINOR Aeroelastic Simulation Code and Its Application to Reduced Vibration Composite Rotor Blade Design," Proceedings of the 50th AIAA/ASME/ASCE/AHS/ACS Structures, Structural Dynamics and Materials Conference, Palm Springs, CA, May 2009. AIAA Paper No. 2009-2601.

13. Myrtle, T. F. and Friedmann, P. P. , "Application of a New Compressible Time Domain Aerodynamic Model to Vibration Reduction in Helicopters Using an Actively Controlled Flap," Journal of the American Helicopter Society, Vol. 46, (1), January 2001, pp. 32–43.

14. Patt, D. , Liu, L. , Chandrasekar, J. , Bernstein, D. S. , and Friedmann, P. P. , "Higher-Harmonic-Control Algorithm for Helicopter Vibration Reduction Revisited," Journal of Guidance, Control, and Dynamics, Vol. 28, (5), September-October 2005, pp. 918–930.

15. Hohenemser, K. H. and Yin, S. , "Some Applications of the Method of Multiblade Coordinates," Journal of American Helicopter Society, Vol. 17, (3), July 1972, pp. 3–12.

16. Padthe, A. K. , Friedmann, P. P. , and Bernstein, D. S. , "Actuator Saturation in Individual Blade Control of Rotorcraft," Proceedings of the 53rd AIAA/ASME/ASCE/AHS/ACS Structures, Structural Dynamics and Materials Conference, Honolulu,HI, April 2012.